https://doi.org/10.1088/1361-6382/abf898

Effects of high density phase transitions on neutron star dynamics

Steven L Liebling^{1,*}, Carlos Palenzuela² and Luis Lehner³

- ¹ Long Island University, Brookville, NY 11548, United States of America
- ² Departament de Física and IAC3, Universitat de les Illes Balears, Palma de Mallorca, Baleares E-07122, Spain
- ³ Perimeter Institute, 31 Caroline St, Waterloo, ON N2L 2Y5, Canada

E-mail: steve.liebling@liu.edu

Received 14 February 2021, revised 29 March 2021 Accepted for publication 15 April 2021 Published 6 May 2021



Abstract

Various theoretical arguments motivate an expectation of a phase transition in matter at extreme densities above nuclear density, accompanied by hopes that gravitational wave observations may reveal the properties of such a transition. Instead of adopting a particular theory, we consider here a generic form of first order phase transition using a piecewise polytropic equation of state, and evolve both isolated neutron stars and neutron star binaries, including unequal mass binaries and, in some cases, magnetic field, looking at dynamical effects. Of particular interest are effects that may be observable either via gravitational waves or electromagnetic observations.

Keywords: neutron stars, gravitational waves, EOS phase transitions

(Some figures may appear in colour only in the online journal)

1. Introduction

Neutron stars are a natural laboratory for matter at extreme densities with their central densities extending to multiples of nuclear density ($\rho_{\rm nuc}=2\times10^{14}~{\rm g~cm^{-3}}$). As such, observations in the gravitational wave (GW) or electromagnetic wave (EM) bands enable a better understanding of the equation of state (EoS) of matter at such high densities. The science obtained from GW observations of the GW170817 [1] and GW190425 [2] binary neutron star mergers by the LIGO/Virgo collaboration along with EM follow up of the former have revealed many aspects of NSs, and results by NICER in the x-ray band have provided important estimates for both the mass and radius of a particular NS (PSR J0030+0451) [3–6].

1361-6382/21/115007+21\$33.00 © 2021 IOP Publishing Ltd Printed in the UK

^{*}Author to whom any correspondence should be addressed.

NSs probe a region of the EoS not well understood. In particular, low densities can be studied in the lab with hadronic matter and extended to higher densities with theoretical extrapolations. At the highest densities, perturbative quantum chromodynamics predicting free quark matter is well accepted. However, between these two regimes there is significant uncertainty and, on fairly general terms, reason to expect (at least one) phase transition (PT). Binary neutron star mergers are of particular relevance to explore this region.

Significant work has studied how such a PT inside an NS might manifest and impact potential observables. In particular, a number of groups have studied numerically the merger of two NSs described by various EoSs with PT. Early work compared the DD2 EoS with a PT to a hyperon phase [7]. Another EoS was studied with a conformally flat, SPH code and found differences in the postmerger oscillation frequencies associated with a PT [8–10]. A similar result with higher postmerger frequencies were found with a PT to quark matter using a fully nonlinear, GR HD code [11–13]. Yet another group studied BNS mergers within an EoS derived from holography, finding lower oscillation frequencies of post-merger remnants [14].

These numerical investigations suggest that more precision in the postmerger regime is needed with GW observatories to observe these PTs, although reference [15] argues that tens of current detections may allow current technology to discern PTs. In contrast though, reference [16] makes an interesting argument with current observations that high mass NSs likely contain a sizable quark matter core.

In this work, with the goal of further identifying potentially relevant features associated with a PT in NSs, we consider one particular EoS in piecewise polytropic form to which we add PTs of different forms. These PTs are not motivated by some particular theory, but instead take a generic approach, subject to mass constraints. We employ them only within regimes in which they remain causal⁴. We then study the dynamics of single stars (which can be rotating and/or magnetized) and the mergers of quasi-circular stellar binaries. This study adds to the body of work on the impacts of PT in BNS—in good agreement with the main qualitative features already observed—as well as considering some novel aspects. In particular, the potential role of magnetic field, increased accretion, and transitions into and out of the PT.

2. Setup

We use the distributed adaptive mesh refinement code MHDuet to evolve the CCZ4 formalism of the Einstein equations coupled to a magnetized perfect fluid, as described in detail in reference [17]. The code is generated with the platform *Simflowny* [18, 19] to run under the SAMRAI infrastructure [20, 21], which allows excellent parallel scaling over thousands of processors. The code has been extensively tested, demonstrating the expected convergence rate of the solutions in different GR and MHD scenarios [17, 22, 23]. MHDuet employs the method of lines, with a fourth-order Runge–Kutta time integrator which ensures the stability and convergence of the solution for time steps smaller than a factor of 0.4 times the grid spacing [24]. The space-time evolution equations are discretized in space using centered finite-difference, fourth-order-accurate operators for the derivatives, and sixth-order Kreiss–Oliger dissipation to filter the high-frequency modes unresolved in our grids. For the fluid, we employ high-resolution shock-capturing methods [25] to deal with the possible appearance of shocks and to take advantage of the existence of weak solutions in the equations. The fluxes at the cell interfaces are calculated by combining the Lax–Friedrich flux splitting formula [26] with the fifth-order, monotonicity-preserving reconstruction method MP5 [27].

⁴ Note that many oft-used EoSs extend into acausal regimes at high densities.

Table 1. Characterization of the different EoSs used in this work. Each EoS is defined as a piecewise polytrope with n=4 segments and with $K_0[\text{CGS}]=3.59389\times 10^{13}$ and $\Gamma_0=1.356$ 92. Each segment is delineated by a transition density ρ_i expressed in cgs units. Note that for the modified SLy, polytropes 1 and 2 have the same value of Γ_i and only the lettered EoSs have a segment with $\Gamma_i=0$.

EoS	Γ_1	Γ_2	Γ_3	$\log_{10} \rho_0$	$\log_{10} \rho_1$	$\log_{10}\rho_2$	$\Delta_{\rho}(\times 10^{14})$
SLy	2.9965	2.9965	2.851	14.165	14.7	14.9367	_
A	2.9965	0.0	2.851	14.165	14.9367	15.1	3.95
В	2.9965	0.0	2.851	14.165	14.9367	15.3	11.3
C	2.9965	0.0	2.851	14.165	14.95	14.97	0.42

In our previous study of neutron star mergers [17] one of the adopted EoSs describing NSs was the SLy EoS, which is still consistent with current observations [3, 28]. Here, our starting point is a modification to this EoS, which we describe with three different piecewise polytropes, as specified in table 1 and displayed in figure 1. We make this modification so that the addition of a PT to the EoS requires only four polytropes, which is the default choice of the code, and refer to this fiducial EoS without the addition of a PT as 'SLy'. Note that with these four polytropes it is already possible to parameterize a wide variety of first order PTs in the EoS, as shown in figure 1.

A piecewise polytrope is chosen such that the pressure is given in terms of the density by

$$p_{\text{cold}}(\rho) = K_i \rho^{\Gamma_i} \tag{1}$$

where i denotes the particular section of the piecewise function and runs from 0 to 3. Enforcing continuity determines the constants K_i .

The PT consists of a section in which $\Gamma_2=0$ beginning at some onset density ρ_1 and extending to some density $\rho_1+\Delta_\rho$, similar to that adopted in references [15, 29]. For this study, the stiffness of the EoS at densities above the transition ($\rho>\rho_1+\Delta_\rho$) remains the same as that for the SLy EoS above ρ_1 , although in principle we are able to modify this as well.

We consider here just a few such variations. The parameters for each EoS are listed in table 1, and we display them in figure 1. In particular, we show the pressure as a function of density which defines a barotropic EoS. We also show in the right panel the family of isolated, spherically symmetric stellar solutions which the EoS generates from solving the TOV equations with Magstar from the Lorene package [30]. One generally expects a change in stability at the extrema of such mass—radius curves. Thus, stars near the region at which the PT occurs (near the cyan circle) are expected to be stable for EoSs A and C, but not B, and the evolutions discussed below (section 3.1) are consistent with this expectation. Also shown is a cyan circle indicating the particular star the evolution of which is discussed below in section 3.1.

Besides the piecewise polytrope, an additional *thermal* component of the EoS is included during the evolution to account for the thermal component of the fluid, represented as an ideal fluid with $\Gamma_{\text{thermal}} = 1.75$. Therefore, the pressure and the internal energy ϵ have two components

$$p = p_{\text{cold}}(\rho) + (\Gamma_{\text{thermal}} - 1) \rho \epsilon_{\text{thermal}}, \tag{2}$$

$$\epsilon = \epsilon_{\text{cold}}(\rho) + \epsilon_{\text{thermal}}.$$
 (3)

At the initial time, $\epsilon_{\text{thermal}}$ vanishes because the initial data relies only upon the piecewise polytrope with $p = p_{\text{cold}}$. We monitor this thermal component in representative cases as another indication of the dynamics.

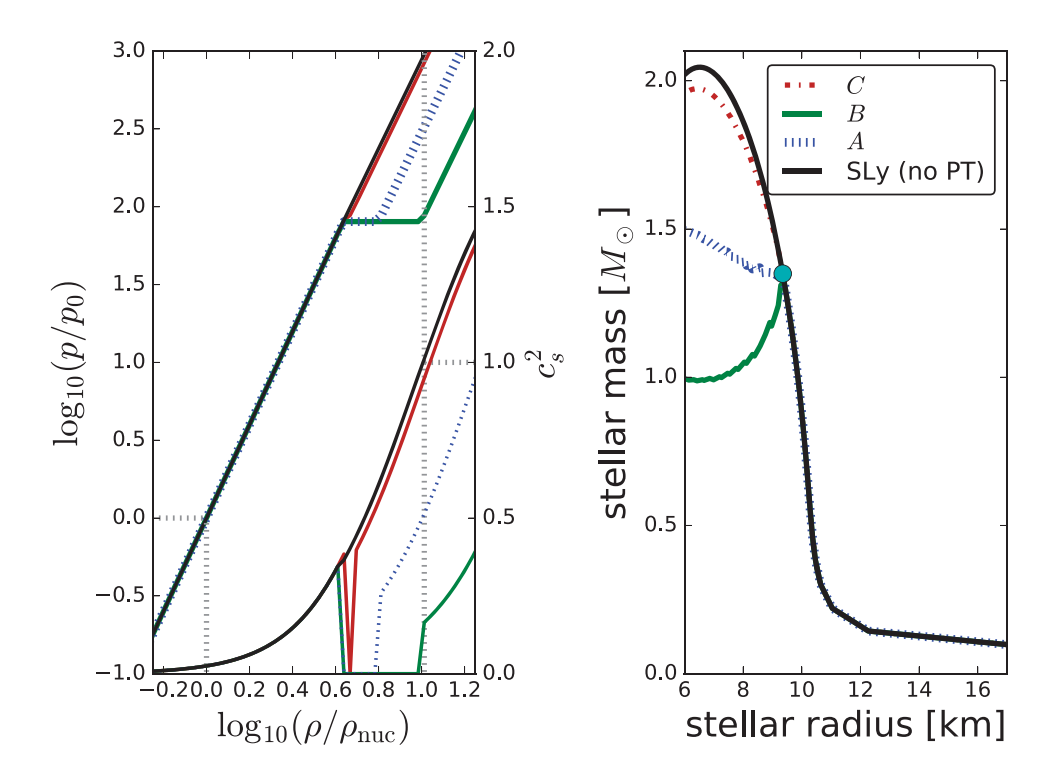


Figure 1. Characterization of the EoSs studied here. Left: standard plot of the pressure versus density for the variations of the base SLy EoS. The pressure p_0 is the pressure at nuclear density as shown with gray dotted lines. The curve for EoS C is difficult to distinguish from SLy because its Δ_{ρ} is so small. Also shown is the sound speed squared (calculated as in equation (4)) for the different EoSs (these are the curves in the bottom right of the panel, contrasting with line segments representing the pressure). Note that only those with a 'strong' PT satisfy $c_s^2 \leqslant 1$, an argument that figures into the recent reference [16]. Right: family of isolated NS solutions (TOV stars) corresponding to each EoS showing the (gravitational) mass versus stellar radius. The cyan circle indicates the particular star evolved in figure 2.

Along with the pressure and the thermal component, the speed of sound as a function of density is calculated for the initial data as

$$c_{\rm s}^2 = \frac{\Gamma_i \, p}{h} \tag{4}$$

where $h = \rho(1 + \epsilon) + p$ is the enthalpy. The sound speed is shown in figure 1 in the same frame as the pressure. The effect of the PT is to decrease the maximum speed of sound attained. Dotted black lines in the left panel of figure 1 indicate the region within which all the EoSs here are causal ($c_s^2 \le 1$), and we note that our evolutions do not probe above this high density regime.

Despite the PT causing the EoS not to be a 1-to-1 function of density, our inversion from conservative to primitive variables causes no numerical problems. We note that the total pressure has both cold and thermal components, and is still a uniquely defined function of the density and internal energy. In particular in solving the transcendental function needed for the inversion, only $p_{\rm cold}$, not its inverse appears, which is unambiguously well defined.

For the magnetized isolated stars studied in this paper, we assume an initially poloidal magnetic field confined to the stellar interior and calculated from the vector potential $A_{\phi} \propto r^2(P-P_{\rm cut})$, where $P_{\rm cut}$ is a 100 times the pressure of the atmosphere (about $2 \times 10^{32} \, {\rm dyn \, cm^{-2}}$) and r is the distance to the rotation axis. The maximum magnetic intensity at the center is $6 \times 10^{13} \, {\rm G}$. We then have the freedom to rotate this configuration some angle, θ , with respect to the rotational axis (here we choose $\theta = 10^{\circ}$).

3. Results

We discuss first the evolutions of isolated stars (spinning or not). Although observable effects are much more likely to arise from the dynamics of binaries than isolated stars, it is informative to study the dynamics of stars in isolation as a first step to fully understand the problem. We have performed evolutions with different resolutions which indicate that the results presented are consistent and within the convergent regime. For example, the finest level covered the isolated stars with approximately 77, 116, and 155 points across the star. Mass was conserved with high accuracy, varying less than a percent during our simulations and improving with resolution. We follow this with a discussion of binary mergers.

3.1. Isolated NSs

Past studies of the evolution of individual stars generally observe stable stars to oscillate around their static solutions because of slight numerical perturbations, or, if unstable, to collapse to black holes. Indeed these two outcomes are observed here. However, to force more significant dynamics, we increase the artificial atmosphere (introduced as part of the standard method of solving for relativistic hydrodynamics) by six orders of magnitude above the usually small level chosen (roughly at the level of $0.3\rho_{\rm nuclear}$). We stress we do not consider such a scenario physically generic, but, in particular, this choice allows us to explore the extent to which possible accretion from a companion can trigger interesting dynamics in a star with an EoS allowing for a PT.

This atmosphere induces strong accretion by the NS (estimated at $\dot{M} \simeq 10^{-8}$). Several important features are observed as a consequence: (i) strong density waves are produced that, as they reach the stellar surface, both reflect an inward propagating wave and expel a thin layer of fluid, (ii) this outer layer sweeps against the atmosphere, essentially halting further accretion for a significant fraction of the stellar dynamical time, and (iii) the propagation speed of such waves is changed significantly in the region where the PT takes place, producing other waves at the interface. The combined impact of these effects plays a strong role regulating the longer term behavior of the star as we discuss below.

In figure 2, we characterize the dynamics of one particular non-rotating star for three different EoSs. The initial data for this star is indicated with a cyan circle on the right panel of figure 1, and, because its maximum density is below the PT onset density (ρ_1 for EoS A and C), it is a solution for all three EoSs.

The top frame shows the maximum density as a function of time for the three evolutions. With no PT, the black curve shows the density oscillate as the star is 'pushed' by the large atmosphere. In contrast, the two evolutions with a PT display large excursions in density consistent with undergoing a PT in the core. For each of the EoSs with a PT, we show the density range over which the PT occurs by a horizontal band, magenta for EoS A and brown for EoS C. These excursions in maximum density generally send the maximum density to a value slightly above each density range.

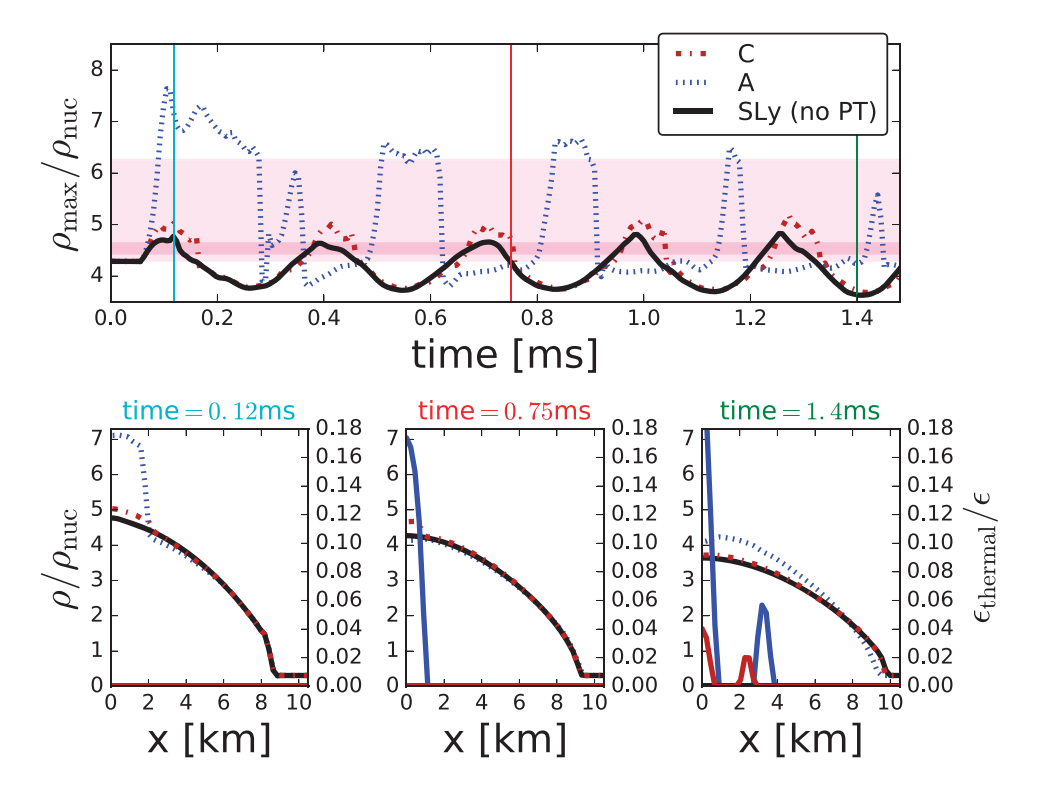


Figure 2. Dynamics of isolated, non-rotating stars. The star represented by a cyan circle in figure 1 is evolved with three different EoSs, and the maximum of the density as a function of time is shown (top). Also shown are two horizontal bands indicating the regions of the PT ($\rho_1 \leqslant \rho \leqslant \rho_1 + \Delta \rho$) for EoS A (magenta) and EoS C (brown). For the SLy EoS with no PT (solid black), the star oscillates as expected. For the EoS A (dotted blue), as the density increases, it shoots past the amplitude of the star with no PT, indicative of the core changing phase. These excursions to hybrid phase ultimately settle back to the hadronic star. At bottom, profiles of the density along the positive x-axis are shown for the three times indicated by vertical lines in the top frame. In the first of these, stars described by EoS A and C have non-hadronic cores. Also shown with the scale on the right is $\epsilon_{\text{thermal}}$ representing the fractional thermal component of the internal energy. These curves can be differentiated from the density both because they are all drawn with solid line and because the thermal energy differs from zero only well inside the star. At early times, the internal energy is entirely comprised of the contribution from the cold component.

It is important to realize that only some inner core undergoes the PT, and we show in the bottom frames of figure 2 the radial profile of the density at three different times. The earliest such profile, when the densities are at their peaks, shows clearly the region containing non-hadronic matter, roughly a region out to 2 km. In some of the later excursions, instead of a convex core of non-hadronic fluid, a small, irregular shell forms such that the density maximum is no longer at the center of the star.

The first panel on the bottom of figure 2 might be misinterpreted as indicating that these stars have different masses despite beginning with the same initial data. A closer look at the total mass, calculated far away from the source, indicates that this is not the case. Furthermore, a simple model can explain how these profiles characterize stars with the same mass. Comparing

the profiles for EoS A and SLy, we assume: (i) the non-hadronic core extends to a radius of roughly 2 km while both stars have radius 8 km, (ii) the non-hadronic core has twice the density of the SLy star, and, finally, (iii) the SLy star has some constant density everywhere, while the EoS A star has a different constant density except in its core. It is straightforward to check that, setting their masses equal and under these assumptions, an overall decrease of roughly 2% in density (if over the entire star) would allow the star to double the density of its inner core, and this difference is roughly consistent with what appears in the figure.

It is interesting to contrast the dynamics of the SLy star with that of EoS A and to wonder why the PT excursions appear damped. As already noted, the generation of thermal energy with EoS A does not appear to play a significant dynamical role given the similarities of the two solutions in the middle frame of figure 2 despite the fact that one has thermal energy present.

One can also consider numerical dissipation, unavoidable in such evolutions. Running at increasing resolutions decreases the expected dissipation, and such tests indicate that dissipation is small and develops slowly in time. Indeed, the size of the non-hadronic core shrinks quickly with each excursion even in the higher resolution runs. Hence, it cannot explain the damped excursions at early times.

If one looks at the radius of the stars as a function of time, one sees that the average radius for both stars increases by about 5% in the first millisecond. Looking at the right panel of figure 1, this increase indicates that the star now oscillates around a slightly different star (slightly smaller gravitational mass) than the one providing the initial data. As the SLy star expands and contracts, its kinetic energy oscillates as well. The EoS A star, on the other hand, has both much less kinetic energy and a less coherent oscillation of it. Instead, the energy provided by the expansion of the star presumably ends up in the non-hadronic core. As the core gets smaller, so does the amount of kinetic energy liberated by exiting the PT. The dearth of kinetic energy at late times in the EoS A star can be seen in the late-time periods in which the maximum density is relatively constant.

At these late times, the EoS A star lacks the coherent motion and kinetic energy present in the SLy star, presumably due to the increased occurrences of characteristics crossing (regions which are handled with a high-resolution shock capturing scheme) as a result of the continuing PTs and the resulting disparate propagation speeds.

We note one final aspect about these non-rotating stars. Our discussion begins with a comment about use of a large atmosphere to force the dynamics, and so here we comment on what is instead seen with the normal, small atmosphere for these stars. The stars once again oscillate, but the amplitude of the oscillations of radius and maximum density instead have amplitude roughly a fraction of a percent. The dynamics for SLy, EoS A, and C are essentially the same with one exception. The maximum density of the star described by EoS A does demonstrate some excursions into the range $\rho_1 < \rho < \rho_1 + \Delta \rho$ but fails to exceed this range. These excursions only occur for some intermediate times once the amplitude of the oscillations have developed and before the star has settled.

We also consider rotating and magnetized stellar evolutions, by setting a small poloidal magnetic field, slightly misaligned with respect to the rotation axis (i.e. 10 degrees), only in the interior of the star. These evolutions also incorporate the same large atmosphere and grid structure as the non-rotating solutions just discussed.

As we discuss later, the onset of the PT introduces non-uniform rotation in the interior of the star which distorts the field topology. However, this distortion takes place deep inside the NS and the matter pressure keeps it confined. As a result, there is essentially no impact on the field behavior within the outer envelope of the NS which implies no direct observational consequences. In figure 3, we once again show the maximum density, and we also show the central magnitude of the magnetic field for a star rotating at a frequency of 800 Hz and with

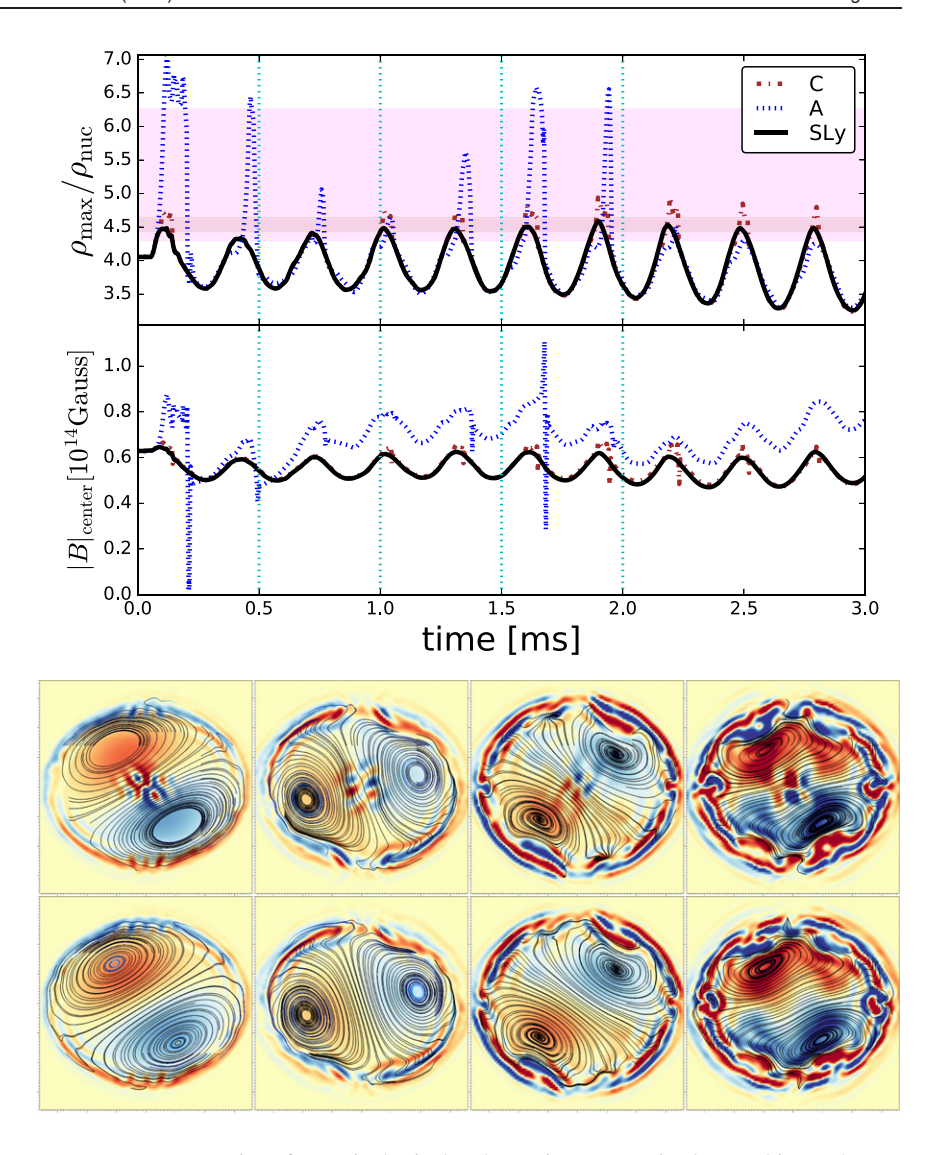


Figure 3. Dynamics of a particular isolated, rotating, magnetized star. This star has an initial central density a bit lower than the lowest density star shown in figure 2 and rotates at 800 Hz. Top: maximum density as a function of time. The star with no PT (black solid) shows the usual stable oscillation. The solid, horizontal, magenta line indicates the onset density of the PT. Middle: the magnitude of the magnetic field at the center as a function of time. Bottom: snapshots of the magnetic field on a meridional plane at times 0.5, 1.0, 1.5, and 2.0 milliseconds (from left to right). The top row of these panels shows EoS A and the bottom row shows the SLy star. The colors indicate the curl of the magnetic field all with the same colormap, and the black lines indicate the magnetic field. Dotted cyan vertical lines are shown in the upper panels indicating the times at which these snapshots are taken. Although the maximum of the magnetic field between the two EoSs looks similar, the structure in the core is significantly different. The passage of the EoS A star through the PT appears to contract the core and result in changes to the magnetic field in the core region. However, these changes do not appear to propagate to the surface.

Table 2. Summary of the neutron star binaries studied here. The initial data were computed using the Bin star solver from the Lorene package [30]. All the binaries start from an initial separation of 37.7 km. The outer boundary is located at 756 km and the highest resolution level covers both stars with a resolution of $\Delta x_{\min} = 100$ m. The table displays the mass ratio of the binary $q \equiv M_1/M_2$, the baryon (gravitational) mass of each star $m_b^{(i)}(m_g^{(i)})$, its circumferential radius $R^{(i)}$ and its compactness $C^{(i)}$ (i.e. when the stars are at infinite separation), the tidal Love numbers of the individual stars, the polarizability parameter of the binary, and the main GW frequency f_2 of the post-merger remnant (displayed in figure 10). Note that binaries with EOSs A and B are not listed because they quickly collapse to black hole.

		M_0^{ADM}	$m_{\rm b}^{(1)}, m_{\rm g}^{(1)}$	$m_{\rm b}^{(2)}, m_{\rm g}^{(2)}$	$R^{(1)}$	$R^{(2)}$						f_2
EoS	q	$[M_{\odot}]$	$[M_{\odot}]$	$[M_{\odot}]$	[km]	[km]	$C^{(1)}$	$C^{(2)}$	$k_2^{(1)}$	$k_2^{(2)}$	κ_2^T	[kHz]
SLy C	1.0	2.471	1.37, 1.20	1.37, 1.20	11.46	11.46	0.1607	0.1607	0.1028	0.1028	119.9	3.02 3.27
SLy C	0.92	2.373	1.37, 1.20	1.25, 1.10	11.46	11.49	0.1607	0.1480	0.1028	0.1122	154.4	3.08 3.02
SLy C	0.86	2.637	1.60, 1.37	1.35, 1.18	11.43	11.46	0.1850	0.1586	0.08484	0.1044	81.23	3.22 3.56

initial central density a bit lower than the onset density. The plot demonstrates a significant difference in magnetic field strength at the center of the star. However, the snapshots of the magnetic field on a meridional plane at four different times shows that the changes within the core do not propagate to the surface. We compare the base EoS with no PT with those of EoS A and C which have a PT but are otherwise stable. When looking at the density, one sees behavior similar to that for the non-rotating case shown in figure 2. That is, the density for each star with the PT has large vertical excursions as the stellar core undergoes the PT. However, the oscillations return the star periodically to a purely hadronic star.

The apparently dramatic excursions of maximum density at late times actually represent the small scale dynamics of the core in which a small region reaches the onset density of the EoS. The cessation of the excursions around $t \approx 2$ ms, however, appears at roughly the time at which the maximum density drifts downward away from the onset density. This drift occurs as well for the star with no PT suggesting that the large scale dynamics is for the star to move towards a different equilibrium.

The bottom panel of figure 3 shows significant differences in the central magnetic field magnitude. Although the magnetic field is likely not affecting the dynamics, it is responding to the changing stellar structure resulting from the transformation of the stellar core to a non-hadronic state. However, we also show the magnetic field lines along a meridional plane at a few different times. The changes in the magnetic field configuration apparent in the figure occur only in the inner part of the star and remain confined to that region as pressure overwhelms any potential propagating effect. On time scales longer than the milliseconds of these evolutions, say of order seconds, such differences might potentially reach the surface. However, the magnitudes of the differences, not so large even in these evolutions, would likely be diminished further as they reach the surface. Without changes to the surface magnetic field, the ability to observe an NS experiencing a PT electromagnetically is likely very limited.

3.2. Binary NSs

We study three particular binaries constructed by Lorene to be in a quasi-circular orbit. These runs use six levels of resolution, the first 5 of which are fixed with a ratio of two between

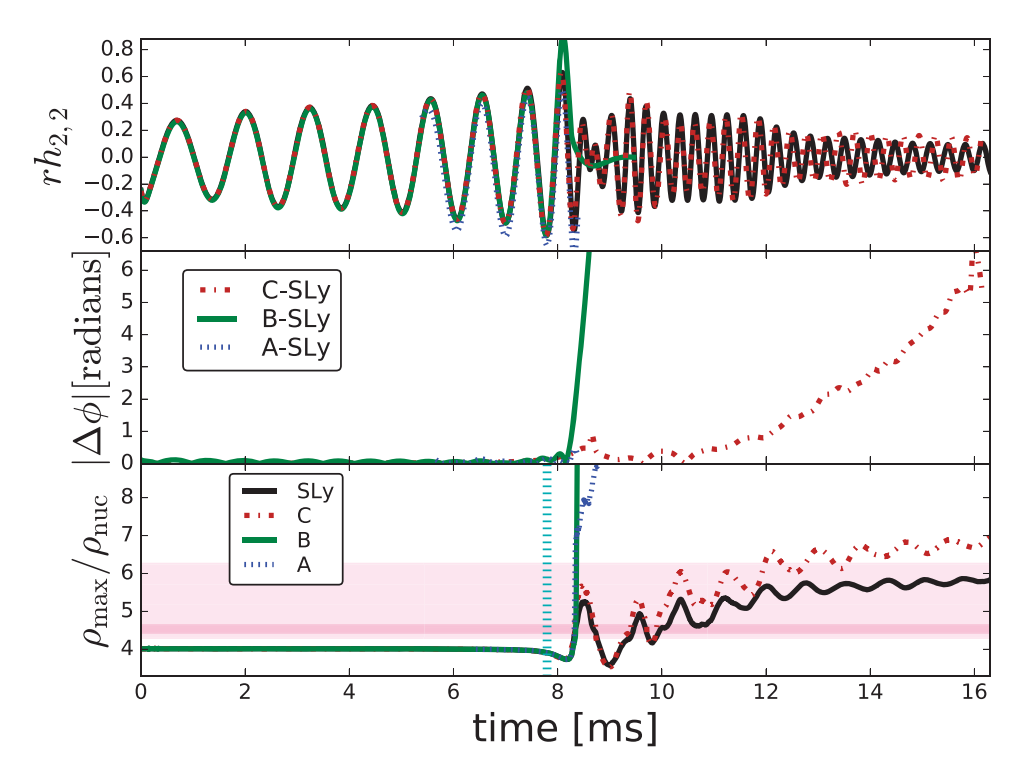


Figure 4. Dynamics of an equal-mass, binary NS merger. Top: the real component of the wavestrain as a function of time. Middle: the difference in phase with respect to the SLy EoS. Bottom: the maximum density as a function of time. The horizontal band indicates the density region in which the PT occurs: wide magenta (EoS A) and thin brown (EoS C). The vertical, cyan line shows the time at which the two stars touch. The mergers with EoSs A and C both result in prompt collapse at merger. The small phase differences at early times are likely due to the double time integration to get the strains and not to any physical effect.

resolutions. The last level is dynamic, tracking the stars, with a refinement ratio of four. The domain extends in each axis from ± 752 km. The finest resolution runs consist of 241^3 points on the coarse level (with a finest level grid spacing of $\Delta x = 98$ m) and others use 193^3 (finest level $\Delta x = 123$ m). For just a few runs and for shorter periods to test that we were in the convergent regime, runs used up to 343^3 points. We note that these binary simulations do not use the large atmosphere adopted for the isolated stars and do not have any magnetization. Certain other details about these binaries are summarized in table 2. Note that these binaries have different total masses which complicates direct comparison among the evolutions. Future work includes constructing binaries maintaining certain parameters, but these variations in total mass allow us to scan a broad range of mass ratio.

We construct an equal mass binary with stellar central densities a bit below the onset density for the EoSs considered here. Once again we consider evolutions with EoSs A, B, C, and SLy (without a PT). The initial data, being below the PT, is the same for all four runs. The total gravitational (or ADM) mass of the system is $2.47M_{\odot}$ and the initial orbital angular velocity is 2190 rad s^{-1} . Each star has a baryonic mass of $M_b = 1.37M_{\odot}$ and is initially separated from the other by 37.73 km.

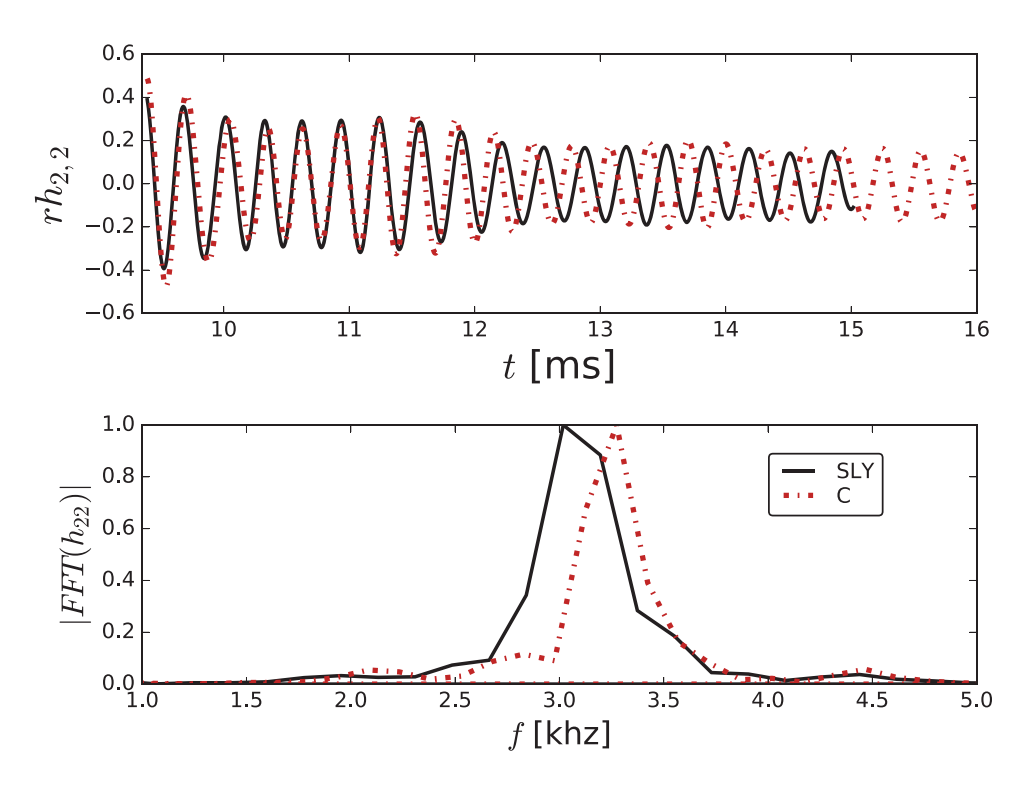


Figure 5. The FFT of the post-merger signals from the equal mass binary mergers shown in figure 4. The power spectral density is shown normalized to the maximum. The remnant that undergoes a PT oscillates at a higher frequency than that without the PT, indicating a more compact remnant.

The evolutions of this binary with different EoSs are displayed in figure 4. The top frame shows the dominant strain mode, $h_{2,2}$ while the middle frame shows the phase difference for each case compared to the EoS with no PT. The bottom frame shows the maximum density, $\rho_{\rm max}$, as a function of time. Within this frame are shown the density bands indicating the PT, thin brown for EoS C and wide magenta for EoS A.

This bottom frame indicates that the binaries apparently share the same evolution at times before merger because the density fails to reach the density at which the EoSs differ. The reader, however, may notice small differences in the strain in the top frame and small phase differences at these pre-merger times. These differences are due to differences arising from the double time integration of ψ_4 over somewhat different time lengths and boundaries. As such, we consider phase differences of order 0.1 radians as something of a floor, and expect physical, and potentially observable, phase differences as those that exceed this floor value.

The binary with the SLy EoS merges and forms a hyper-massive neutron star which remains stable for at least 10 ms after the collision. The cases with a PT depart from this behavior.

It is not at all surprising that the result for EoS B collapses promptly at merger based on the stability properties of the EoS at high mass. This expectation can be explained by examining the TOV solutions associated with EoS B as plotted in the right frame of figure 1. A local maximum occurs in the mass-versus-radius plot right near the region describing hybrid solutions and such an extremum indicates a change in stability; in contrast, the other EoSs do not have an extremum in that region.

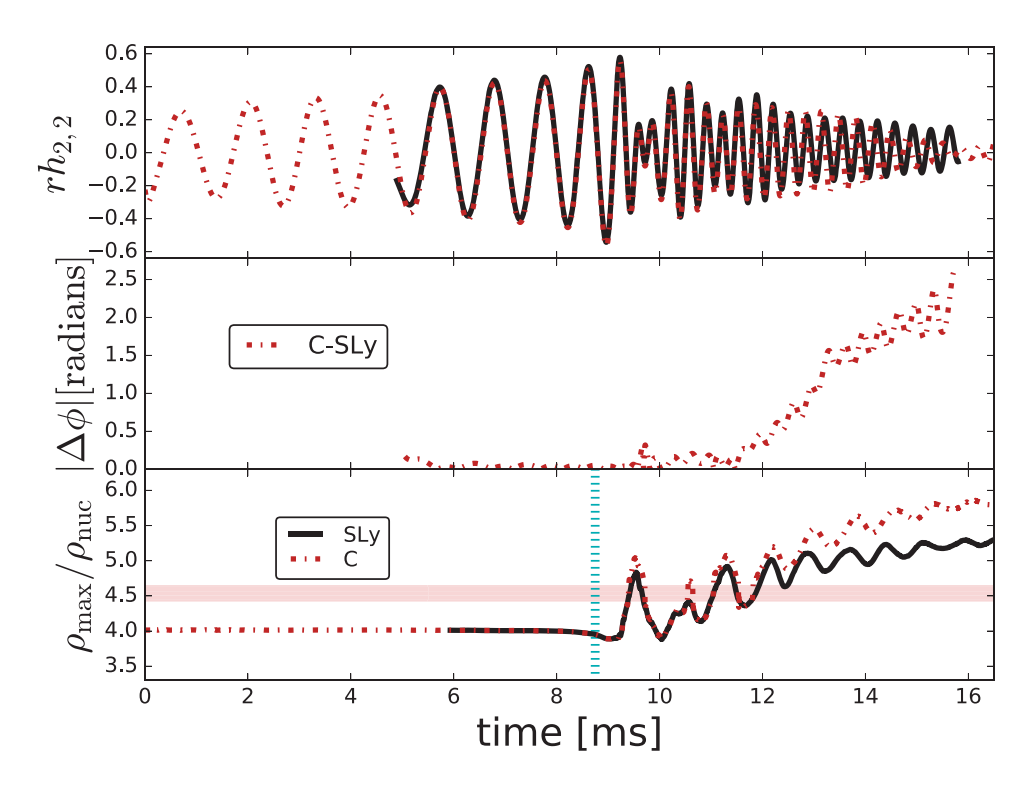


Figure 6. Dynamics of the q=0.92 unequal-mass, binary NS merger with masses $1.2M_{\odot}$ and $1.1M_{\odot}$. The vertical, cyan line shows the time at which the two stars touch.

We also observe the binary described by EoS A collapsing quickly upon merger. Again, by examining the TOV solutions in the right frame of figure 1 one can clearly see that EoS A does not support as massive stars as EoS C, and one expects the remnant to be fairly massive.

The remnant under EoS C survives the merger, and, once the maximum density increases after the stars merge (see bottom panel of figure 4), the GW signal shows differences (see the middle panel showing the phase difference between the GW signals). However, not until a bit more than 2 ms after merger does the phase difference between EoS C and SLy begin to grow steadily.

Because the GW differences occur post-merger, we analyze the frequency differences with a fast-Fourier-transform (FFT) of just the post-merger region of the signal. We show this FFT and the signals in this region in figure 5. The remnant with the PT oscillates at a higher frequency consistent with the results of reference [11–13]. Such a behavior can be understood in terms of a simple model. In the equal mass case, the PT takes place at a central region in the remnant. There, the density is higher and, as a consequence of its moment of inertia decreasing (due to approximate mass conservation), the angular frequency goes up. In cases where such a region is sufficiently large, its contribution to GWs from the system dominates. Thus, there is a tendency towards higher frequencies due to the PT.

We next consider unequal mass binaries. The study of asymmetric BNS binaries has become yet more relevant and interesting in light of the recent observation of a BNS with asymmetric

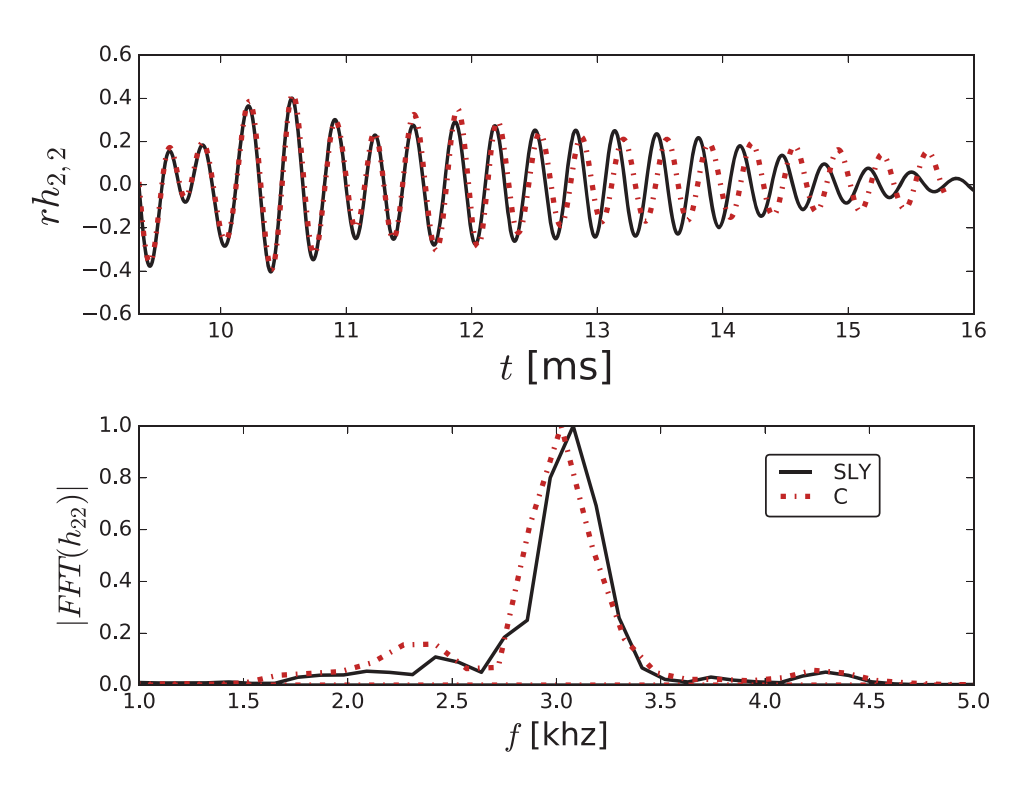


Figure 7. The FFT of the post-merger signals from the q=0.92 unequal mass binary mergers shown in figure 6. The power spectral density is shown normalized to the maximum.

mass ratio of q = 0.78 via pulsar timing [31]. First, we consider one with mass ratio⁵ q = 0.92 shown in figure 6.

In this case, the overall qualitative behavior is very similar to the equal mass case. Importantly however, the main frequency in the GWs produced post-merger, as shown in figure 7, is quite close for both the purely hadronic and PT cases. Two factors help explain why the post-merger frequencies are closer together than in the q=1 case. The first is that the non-hadronic core for this remnant is smaller than that formed in the equal mass case and therefore presumably contributes little to increasing the rotational frequency via conservation of angular momentum. This is related to the fact that this binary reaches the smallest post-merger densities of these binaries (see figure 11 discussed below). The other factor is a bit more subtle and particular to the unequal mass case. Unlike the 'dumbbell' formed in the early merger of the equal mass case, the remnant of an unequal mass merger is dominated by the more massive object which happens to contain the non-hadronic core. As the core gets closer to the rotational axis, its contribution to GW production decreases and its own quadrupole moment begins to be the dominant effect.

Next, we study a case with q = 0.86. The idea here was to construct a binary with one hybrid star that has a maximum density above the PT of the EoS while the other is a normal hadronic star with lower central density. This high mass star could potentially undergo the PT in the

⁵ We define the mass ratio in terms of the two gravitational masses of the binary components with $M_{\rm g}^2 \geqslant M_{\rm g}^1$ and $q \equiv M_{\rm g}^1/M_{\rm g}^2$.

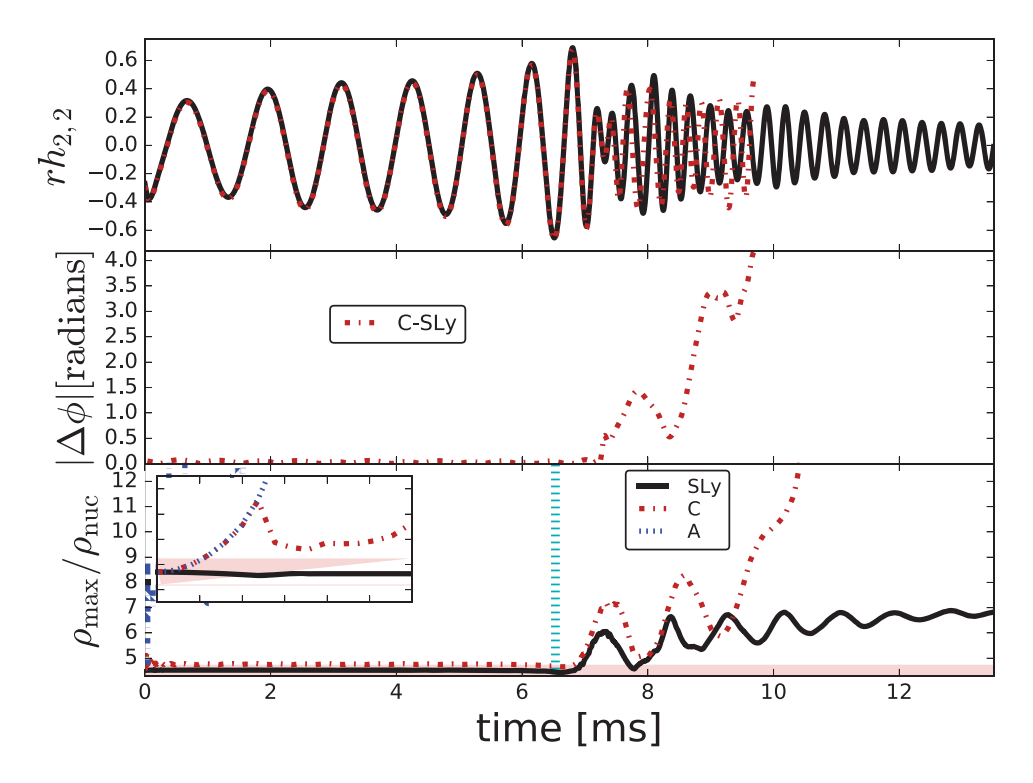


Figure 8. Dynamics of a q=0.86, unequal-mass, binary NS merger with masses $1.37M_{\odot}$ and $1.18M_{\odot}$. This binary lacks a PT in the ID because Lorene seems unable to produce a binary with one hadronic star and one with a non-hadronic core. However, the density of the high mass star is such that the evolution quickly shows it to go through the PT, as shown in the inset which covers the period $0 \le t \le 0.06$ ms. One is then evolving a binary with one hybrid star and one hadronic. The vertical, cyan line shows the time at which the two stars touch.

opposite sense as those described above. However, we were not able to generate such a binary with Lorene, and so instead we started with a purely hadronic, unequal mass binary. Note, this difficulty arises only for this mass ratio, not the previously presented cases. However, we stress that the choice of a sufficiently massive star leads to the PT taking place dynamically and the resulting binary is of mixed type. Indeed, once evolved with EoS A or C, the higher mass star quickly undergoes the PT (see the inset of the bottom panel of figure 8 showing the early time behavior of the maximum density).

As shown in figure 8, the maximum density at early times shows large differences among the three EoSs. With EoS SLy, the binary evolves without any significant change to the maximum density. In contrast, both EoS A and C show a quick rise in the maximum density indicating that the stars are undergoing their respective PT. The high mass star with EoS A quickly collapses. As shown in figure 9, the post-merger differences resemble those in the equal mass case with the EOS C remnant oscillating at a higher frequency.

Common to all three binaries studied here, the maximum density decreases just after the stars touch and just before merger (see the bottom panels just after the vertical cyan line in figures 4, 6 and 8). This decrease in maximum density for all the binaries considered here is also shown in figure 11. Such a decrease is already expected from post Newtonian calculations (e.g. [32]) and has potentially important consequences. For stars above the PT, the drop in maximum

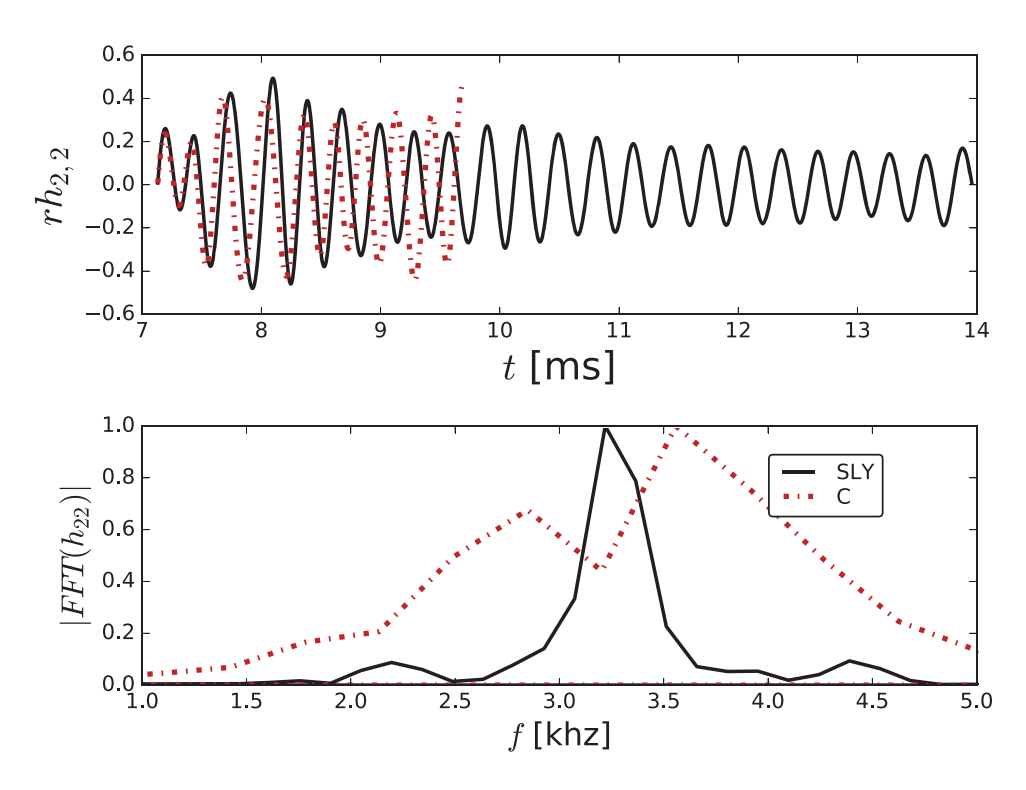


Figure 9. The FFT of the post-merger signals from the q=0.86 unequal mass binary mergers shown in figure 8. The power spectral density is shown normalized to the maximum.

density does not appear significant enough for the star to drop through the PT to a purely hadronic star *before* the stars come into contact (behavior already indicated by PN arguments where $\delta\rho_{\rm c}/\rho_{\rm c}\lesssim 0.3\%$ in e.g. the equal mass case). However, the trend towards a decrease in central density continues up to $\delta\rho_{\rm c}/\rho_{\rm c}\simeq 2\%$ (for the equal mass case, see figure 11). Such a decrease could imply a transition back to a purely hadronic case for stars barely above the PT. After such transitory density minima, strong density oscillations could potentially have a correlated behavior 'in and out' of the PT for some time (akin to the oscillations discussed before in the case of isolated neutron stars). However, this scenario might only arise within a narrow set of physical parameters.

Let us now take a closer look at the dependence of the main frequency, f_2 , of the post-merger GW signal with the effective 'remnant tidal polarizability parameter', κ_2^T , defined as

$$\kappa_2^T = 2 \left[q \left(\frac{X^{(1)}}{C^{(1)}} \right)^5 k_2^{(1)} + \frac{1}{q} \left(\frac{X^{(2)}}{C^{(2)}} \right)^5 k_2^{(2)} \right],$$
(5)

where $q = M^{(2)}/M^{(1)} \le 1$, $X^{(i)} = M^{(i)}/(M^{(1)} + M^{(2)})$ and $C^{(i)} = M^{(i)}/R^{(i)}$, being $k_2^{(i)}$ the individual tidal Love numbers of each star. A rather robust functional dependence has been found that relates these two quantities (e.g. [34–36]). Figure 10 displays a particular fit of this frequency as a function of this polarizability parameter, obtained by extracting this value from

⁶ Also known as one of a family of 'dimensionless tidal parameters' in the effective one body approach [33].

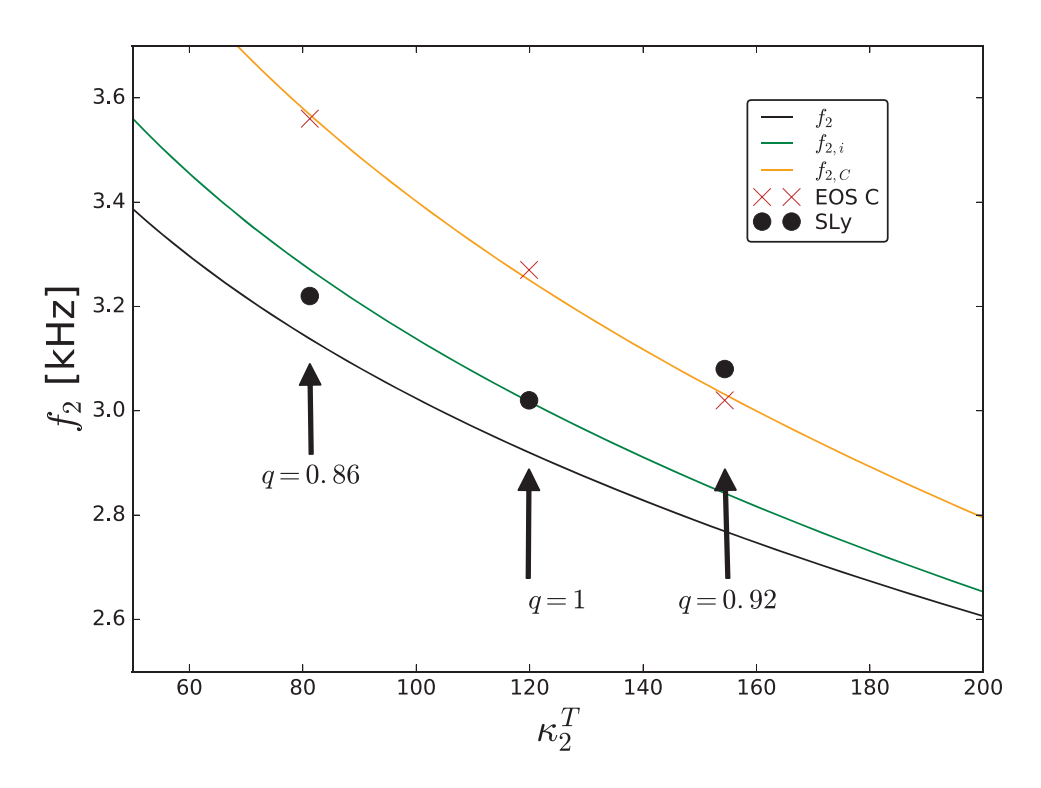


Figure 10. Post-merger f_2 frequencies for the various binaries studied here along with fits to these frequencies. The fits $f_2 = 5.832 - 1.118 \left(\kappa_2^T\right)^{1/5}$ and $f_{2,i} = 6.401 - 1.299 \left(\kappa_2^T\right)^{1/5}$ come from reference [37]. The frequencies for EoS C appear to follow a similar trend, and a fit to just these three points with the same form results in $f_{2,C} = 7.482 - 1.624 \left(\kappa_2^T\right)^{1/5}$.

the remnant of many binary neutron star simulations, with different EoS without a PT [37]. We include on the figure our values for our modified SLy and those obtained with EoS C computed from the FFTs of the postmerger signals. Because we evolve our binaries just a few milliseconds after merger, we also include the frequency fit $f_{2,i}$ which represents the transient frequency just after merger.

The equal mass (q=1) and q=0.86 cases show significant differences in the post-merger frequencies, which could potentially identify the PT (see e.g. reference [8]). As noted, the q=0.92 case shows a small difference; restricting the FFT to times after 13 ms shows that the f_2 frequency for EoS C is arguably consistent to that of the case without the PT.

It is not completely clear how complicated the dependence of the post-merger frequency may be when PTs are involved, and the impact of both mass ratio and total mass of the binary. More thorough coverage of the parameter space would be needed to construct a model able to predict the expected values of f_2 in general cases. Despite this need for more coverage, the frequencies obtained for EoS C do appear to follow a similar functional form as that obtained for EoSs with no PT, and we present that fit in the figure.

Another aspect of the binary merger that may lead to differences due to the presence of a PT is the development of the m=1 mode [38, 39]. This mode grows more quickly for unequal mass binaries, and so the wide range of mass ratios in our simulations does well to probe for such differences. In figure 12, we compare the magnitude of the $\Psi_4^{2,1}$ mode for SLy and

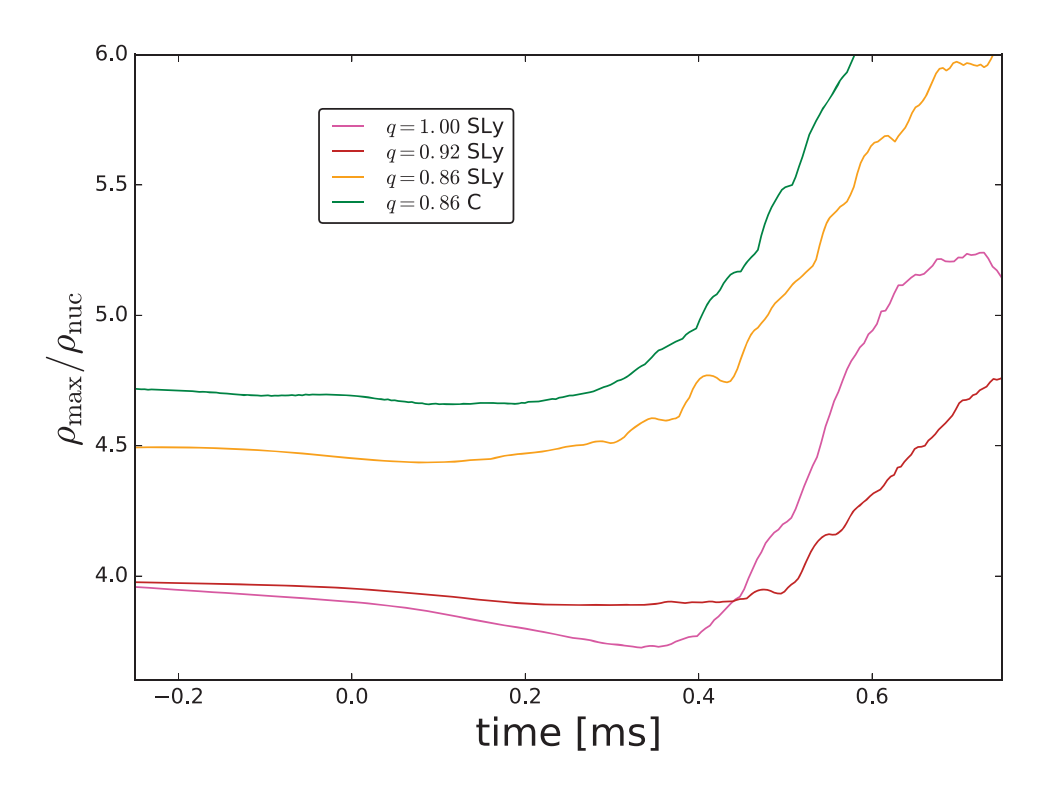


Figure 11. Near-merger behavior of maximum density for the various binaries studied here. The times for all binaries have been shifted such that t = 0 denotes the moment when the stars first touch. The maximum density dips soon after the stars touch.

EoS C with the q = 0.92 mass ratio, our longest post-merger evolution and one that typifies the differences in the other two cases. As shown in the figure, the mode for each case grows qualitatively similarly, suggesting that the PT does not significantly affect the growth rate of this instability.

4. Discussion

We compare evolutions of NSs and BNSs with EoSs that differ only in the presence of a somewhat generic PT. That is, the PT is arbitrary and not motivated by a particular theory of high density matter. Only a few different PTs are adopted among a large space of possibilities.

With individual NSs, hadronic stars with core densities close to the PT can undergo the PT and oscillate between hadronic and hybrid states. The dynamics of this oscillation appears to involve a complex interplay of a few factors. The star expands and contracts, generates thermal energy, and all the while the fraction of the core becoming non-hadronic decreases. This behavior arises from the accretion and pressure afforded by the artificially high atmosphere chosen here that is likely unrealistic. However this interesting behavior might instead be triggered astrophysically. For example, it would be interesting to assess whether the onset of this behavior might be induced by strong tidal interactions in an eccentric binary as explored in [40].

With rotation and magnetic field, the core is similarly dynamic. However, we observe no significant change to the surface magnetic field.

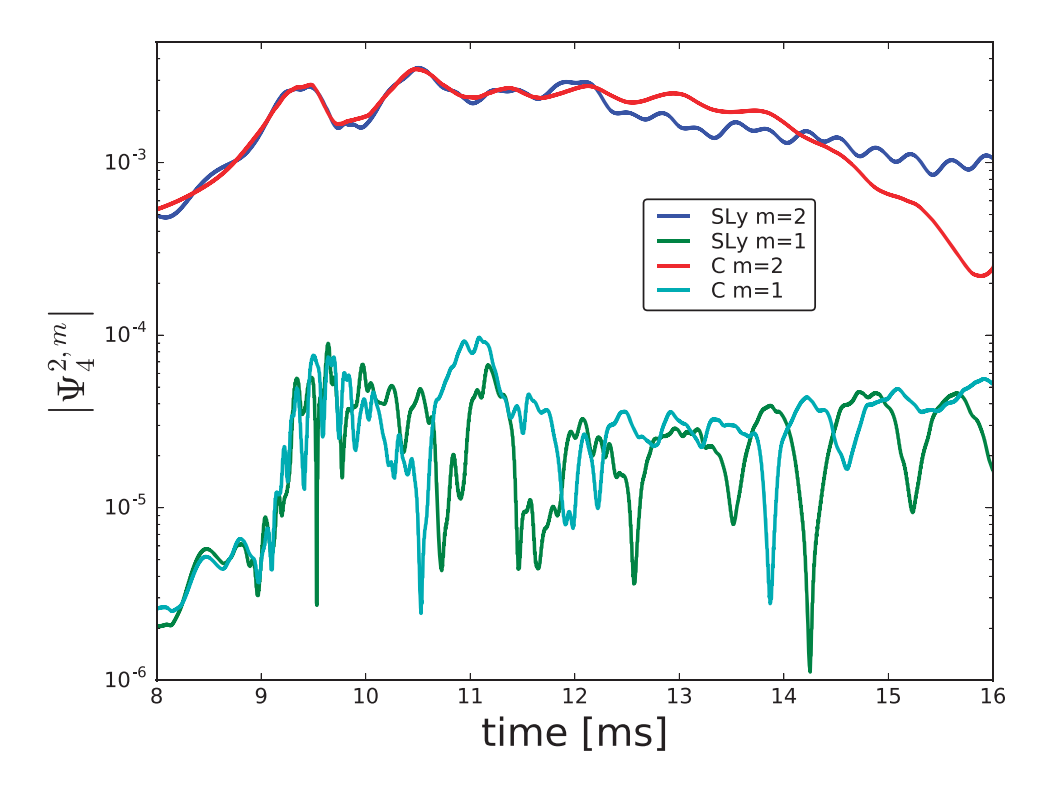


Figure 12. Comparison of the growth of the m=1 mode for the q=0.92 binary postmerger. The growth of this mode, although different between the two EoSs, is roughly comparable.

Evolutions of binary mergers of hadronic stars with densities close to the onset density of a PT, both equal and unequal masses show a difference in their GW signatures at merger when the maximum density reaches the onset density. The phase difference increases as the post-merger regime continues and the remnant oscillates at higher frequency than the hadronic remnant. We expect that, at least in some cases, these differences may be observable, although one can imagine possible degeneracies with EOSs lacking a PT but that otherwise produce condensed cores at high densities.

We also consider the novel scenario of a BNS composed of a hybrid star along with a hadronic star. Such a necessarily unequal mass binary, here with q=0.86, is particularly relevant given the recent detections via pulsar timing of a very unequal (q=0.78) BNS [31] and with asymmetric compact object binaries by LIGO/Virgo. A binary such as this offers the possibility that the hybrid star decompresses and becomes more hadronic dynamically. Although our q=0.86 binary is composed of a hybrid and a hadronic star, this binary collapsed to a black hole at merger. However, were a PT occurring at smaller density chosen, one could then construct such a scenario that avoided collapse at merger.

We also computed the dominant post-merger oscillation frequency of the remnant for these mergers. Future generations of GW observatories are expected to have a bandwidth extending to the post-merger regime with the hope of differentiating a PT in the EoS via these frequency differences. Further theoretical analysis of the many outcomes will be required to guide detection efforts as well as development of efficient ways to search for such subtle observables, e.g. [41, 42].

Acknowledgments

We would like to thank Will East for helpful discussions and to Juan Calderon for addressing our attention to the effects of PT on the m=1 instability. This work was supported by the NSF under Grants PHY-1912769 and PHY-2011383. CP acknowledges support from the Spanish Ministry of Economy and Competitiveness Grants AYA2016-80289-P and PID2019-110301GB-I00 (AEI/FEDER, UE). LL was supported in part by NSERC through a Discovery Grant, and CIFAR. Computations were performed at XSEDE, Marenostrum and the Niagara supercomputer at the SciNet HPC Consortium. Computer resources at MareNostrum and the technical support provided by Barcelona Supercomputing Center were obtained thanks to time granted through the 17th (Project Tier-0 GEEFBNSM) and 20th (Proposal 2019215177) PRACE regular calls. SciNet is funded by: the Canada Foundation for Innovation; the Government of Ontario; Ontario Research Fund—Research Excellence; and the University of Toronto. Research at Perimeter Institute is supported by the Government of Canada and by the Province of Ontario through the Ministry of Research, Innovation and Science.

Data availability statement

No new data were created or analysed in this study.

ORCID iDs

Steven L Liebling https://orcid.org/0000-0002-5008-6119 Carlos Palenzuela https://orcid.org/0000-0003-0634-531X Luis Lehner https://orcid.org/0000-0001-9682-3383

References

- [1] Virgo, LIGO Scientific Collaboration 2017 GW170817: observation of gravitational waves from a binary neutron star inspiral *Phys. Rev. Lett.* 119 161101
- [2] Abbott B et al (LIGO Scientific, Virgo Collaboration) 2020 GW190425: observation of a compact binary coalescence with total mass ~3.4M_☉ Astrophys. J. Lett. 892 L3
- [3] Miller M C et al 2019 PSR J0030+0451 mass and radius from NICER data and implications for the properties of neutron star matter Astrophys. J. Lett. 887 L24
- [4] Riley T E et al 2019 A NICER view of PSR J0030+0451: millisecond pulsar parameter estimation Astrophys. J. Lett. 887 L21
- [5] Bogdanov S et al 2019 Constraining the neutron star mass—radius relation and dense matter equation of state with NICER. II. Emission from hot spots on a rapidly rotating neutron star Astrophys. J. 887 L26
- [6] Bilous A V et al 2019 A NICER view of PSR j0030+0451: evidence for a global-scale multipolar magnetic field Astrophys. J. 887 L23
- [7] Radice D, Bernuzzi S, Pozzo W D, Roberts L F and Ott C D 2017 Probing extreme-density matter with gravitational-wave observations of binary neutron star merger remnants Astrophys. J. 842 L 10
- [8] Bauswein A, Bastian N-U F, Blaschke D B, Chatziioannou K, Clark J A, Fischer T and Oertel M 2019 Identifying a first-order phase transition in neutron star mergers through gravitational waves Phys. Rev. Lett. 122 061102
- [9] Bauswein A et al 2019 Equation-of-state constraints and the QCD phase transition in the era of gravitational-wave astronomy AIP Conf. Proc. 2127 020013

- [10] Blacker S, Bastian N-U F, Bauswein A, Blaschke D B, Fischer T, Oertel M, Soultanis T and Typel S 2020 Constraining the onset density of the hadron–quark phase transition with gravitational-wave observations *Phys. Rev.* D 102 123023
- [11] Most E R, Papenfort L J, Dexheimer V, Hanauske M, Schramm S, Stöcker H and Rezzolla L 2019 Signatures of quark–hadron phase transitions in general-relativistic neutron-star mergers *Phys. Rev. Lett.* 122 061101
- [12] Most E R, Papenfort L J, Dexheimer V, Hanauske M, Stöcker H and Rezzolla L 2019 On the deconfinement phase transition in neutron-star mergers (arXiv:1910.13893 [astro-ph.HE])
- [13] Weih L R, Hanauske M and Rezzolla L 2020 Postmerger gravitational-wave signatures of phase transitions in binary mergers Phys. Rev. Lett. 124 171103
- [14] Ecker C, Järvinen M, Nijs G and van der Schee W 2020 Gravitational waves from holographic neutron star mergers Phys. Rev. D 101 103006
- [15] Chen H-Y, Chesler P M and Loeb A 2020 Searching for exotic cores with binary neutron star inspirals Astrophys. J. Lett. 893 L4
- [16] Annala E, Gorda T, Kurkela A, Nättilä J and Vuorinen A 2019 Quark-matter cores in neutron stars (arXiv:1903.09121 [astro-ph.HE])
- [17] Liebling S, Palenzuela C and Lehner L 2020 Towards fidelity and scalability in non-vacuum mergers (arXiv:2002.07554 [gr-qc])
- [18] Arbona A, Artigues A, Bona-Casas C, Massó J, Miñano B, Rigo A, Trias M and Bona C 2013 Simflowny: a general-purpose platform for the management of physical models and simulation problems *Comput. Phys. Commun.* 184 2321–31
- [19] Arbona A, Miñano B, Rigo A, Bona C, Palenzuela C, Artigues A, Bona-Casas C and Massó J 2018 Simflowny 2: an upgraded platform for scientific modelling and simulation *Comput. Phys. Commun.* 229 170–81
- [20] Hornung R D and Kohn S R 2002 Managing application complexity in the SAMRAI object-oriented framework Concurr. Comput.: Pract. Exp. 14 347–68
- [21] Gunney B T N and Anderson R W 2016 Advances in patch-based adaptive mesh refinement scalability J. Parallel Distrib. Comput. 89 65–84
- [22] Palenzuela C, Miñano B, Viganò D, Arbona A, Bona-Casas C, Rigo A, Bezares M, Bona C and Massó J 2018 A Simflowny-based finite-difference code for high-performance computing in numerical relativity Class. Quantum Grav. 35 185007
- [23] Viganò D, Aguilera-Miret R, Carrasco F, Miñano B and Palenzuela C 2020 General relativistic MHD large eddy simulations with gradient subgrid-scale model *Phys. Rev.* D 101 123019
- [24] Butcher J C 2008 Numerical Methods for Ordinary Differential Equations (New York: Wiley) http://dx.doi.org/10.1002/9780470753767.fmatter
- [25] Toro E F 1999 Riemann Solvers and Numerical Methods for Fluid Dynamics: A Practical Introduction 2nd edn (Berlin: Springer) http://cds.cern.ch/record/404378
- [26] Shu C-W 1998 Essentially Non-oscillatory and Weighted Essentially Non-oscillatory Schemes for Hyperbolic Conservation Laws (Berlin: Springer) pp 325–432 https://doi.org/10.1007/ BFb0096355
- [27] Suresh A and Huynh H T 1997 Accurate monotonicity-preserving schemes with Runge-Kutta time stepping J. Comput. Phys. 136 83–99
- [28] Abbott B et al (LIGO Scientific, Virgo Collaboration) 2018 GW170817: measurements of neutron star radii and equation of state Phys. Rev. Lett. 121 161101
- [29] Lindblom L 1998 Phase transitions and the mass radius curves of relativistic stars Phys. Rev. D 58 024008
- [30] Gourgoulhon E, Grandclément P, Marck J-A, Novak J and Taniguchi K 2010 Lorene home page http://lorene.obspm.fr/
- [31] Ferdman R D *et al* 2020 Asymmetric mass ratios for bright double neutron-star mergers *Nature* **583** 211–4
- [32] Lai D 1996 Tidal stabilization of neutron stars and white dwarfs Phys. Rev. Lett. 76 4878-81
- [33] Damour T and Nagar A 2010 Effective one body description of tidal effects in inspiralling compact binaries Phys. Rev. D 81 084016
- [34] Bernuzzi S, Nagar A, Balmelli S, Dietrich T and Ujevic M 2014 Quasiuniversal properties of neutron star mergers Phys. Rev. Lett. 112 201101
- [35] Lehner L, Liebling S L, Palenzuela C, Caballero O L, O'Connor E, Anderson M and Neilsen D 2016 Unequal mass binary neutron star mergers and multimessenger signals Class. Quantum Grav. 33 184002

- [36] Vretinaris S, Stergioulas N and Bauswein A 2020 Empirical relations for gravitational-wave asteroseismology of binary neutron star mergers Phys. Rev. D 101 084039
- [37] Rezzolla L and Takami K 2016 Gravitational-wave signal from binary neutron stars: a systematic analysis of the spectral properties *Phys. Rev.* D 93 124051
- [38] Paschalidis V, East W E, Pretorius F and Shapiro S L 2015 One-arm spiral instability in hypermassive neutron stars formed by dynamical-capture binary neutron star mergers (arXiv:1510.03432 [astro-ph.HE])
- [39] Lehner L, Liebling S L, Palenzuela C and Motl P M 2016 m=1 instability and gravitational wave signal in binary neutron star mergers *Phys. Rev.* D **94** 043003
- [40] Yang H, East W E, Paschalidis V, Pretorius F and Mendes R F 2018 Evolution of highly eccentric binary neutron stars including tidal effects *Phys. Rev.* D 98 044007
- [41] Yang H, Paschalidis V, Yagi K, Lehner L, Pretorius F and Yunes N 2018 Gravitational wave spectroscopy of binary neutron star merger remnants with mode stacking *Phys. Rev.* D **97** 024049
- [42] Whitaker T, East W E, Green S, Lehner L and Yang H 2021 Phenomenological waveforms for post-merger binary neutron stars with artificial neural networks (in preparation)